

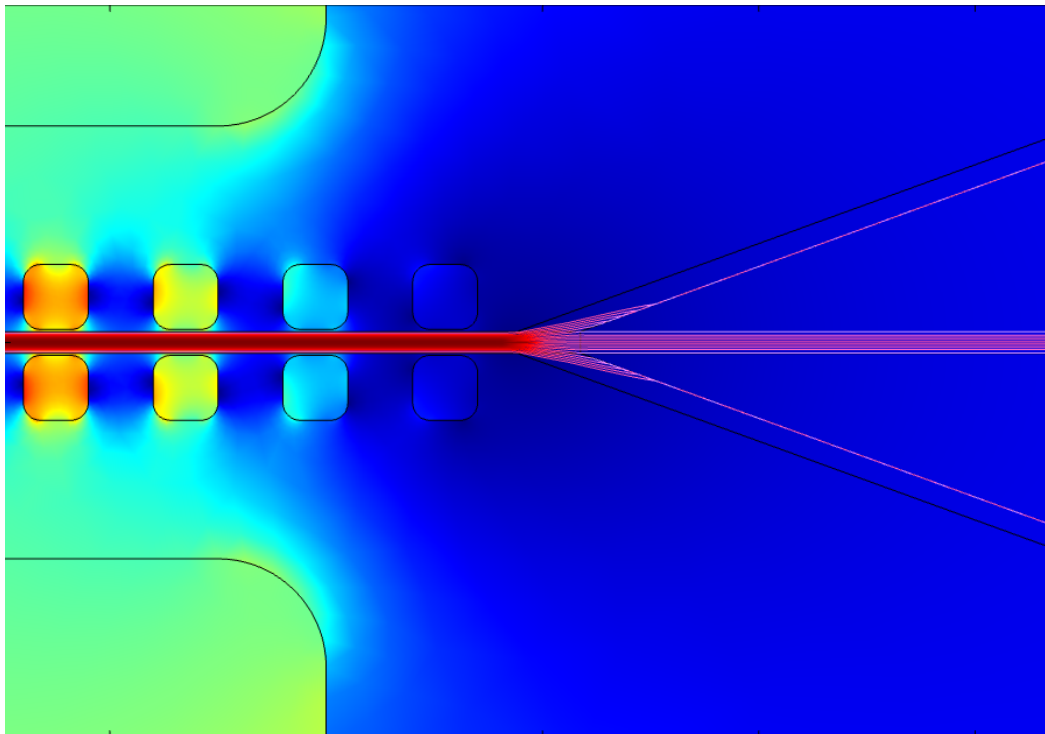
*BEE 4530 Group 4*

---

# Optimizing Throughput in a Fetal Cell Magnetophoretic Separator

---

*Zachary Flood, Naveen Jasty, Chiyu Jiang, Jino Park*



May 14, 2015

## Contents

<b>1</b>	<b>Executive Summary</b>	<b>4</b>
<b>2</b>	<b>Introduction</b>	<b>5</b>
<b>3</b>	<b>Design Objectives</b>	<b>6</b>
<b>4</b>	<b>Schematic</b>	<b>6</b>
4.1	Device . . . . .	6
4.2	Mesh . . . . .	8
<b>5</b>	<b>Theory</b>	<b>10</b>
5.1	Magnetostatics . . . . .	10
5.1.1	Governing Equations . . . . .	10
5.1.2	Boundary Conditions . . . . .	10
5.2	Fluid Dynamics . . . . .	11
5.2.1	Governing Equations . . . . .	11
5.2.2	Boundary Conditions . . . . .	11
5.3	Motion . . . . .	11
5.3.1	Governing Equations . . . . .	11
<b>6</b>	<b>Results</b>	<b>12</b>
6.1	Original Design . . . . .	12
6.1.1	Fluid Simulation . . . . .	12
6.1.2	Magnetic Field Simulation . . . . .	13
6.1.3	Particle Tracing . . . . .	14
6.2	Flow Rate Optimization For Efficient Throughput . . . . .	16
6.2.1	Objective Function . . . . .	16
6.2.2	Results from Objective Function Evaluation . . . . .	17
6.3	New Design with New Flow Channel Geometry . . . . .	17
<b>7</b>	<b>Sensitivity Analysis</b>	<b>19</b>
7.1	Parameters to Adjust . . . . .	19
7.2	Sensitivity to Input Parameters . . . . .	19
7.2.1	Blood Viscosity . . . . .	19
7.2.2	Blood Density . . . . .	19
7.2.3	Magnetic Field Strength . . . . .	19
7.2.4	Soft Element Width . . . . .	20
7.3	Sensitivity Summary . . . . .	20
<b>8</b>	<b>Accuracy Check</b>	<b>20</b>
8.1	Verification . . . . .	21
8.2	Validation . . . . .	22
<b>9</b>	<b>Conclusion</b>	<b>24</b>
9.1	Future Work . . . . .	25
<b>10</b>	<b>Contributions</b>	<b>25</b>

<b>11 Appendices</b>	<b>26</b>
11.1 Input Parameters . . . . .	26
11.2 Variable Definitions . . . . .	26
<b>References</b>	<b>27</b>

## List of Figures

1	Schematic . . . . .	7
2	Mesh convergence . . . . .	8
3	Full mesh view . . . . .	9
4	Magnified mesh view . . . . .	9
5	Fluid velocity contour plot . . . . .	12
6	Fluid pressure along channel center-line . . . . .	13
7	Magnetic flux density contour plot . . . . .	13
8	Gradient of magnetic flux density contour plot . . . . .	14
9	Application of magnetophoretic force . . . . .	15
10	Separation particle tracks . . . . .	15
11	Objective function vs. flow velocity . . . . .	17
12	Proposed design . . . . .	18
13	Improved separation particle tracks . . . . .	18
14	Magnetic flux density along channel length . . . . .	22
15	Magnetophoretic force along channel length . . . . .	23
16	Magnetophoretic force across the channel . . . . .	24

## List of Tables

1	Sensitivity Analysis Summary . . . . .	20
2	Input Parameters . . . . .	26
3	Variable Definitions . . . . .	26

## 1 Executive Summary

Magnetophoretic separation is a non-invasive method under development for the sampling of nucleated fetal red blood cells (NRBCs). By inducing a magnetic field gradient symmetrically about a microfluidic separatory channel, blood cells may be separated based on their inherent magnetic properties [1]. Diamagnetic red blood cells (RBCs) are magnetically attracted into lateral side channels, while others cells, e.g. white blood cells (WBCs), are paramagnetic and repelled into the center waste channel. We aimed to model the first phase of a complete lab-on-chip device for the separation of RBCs from maternal circulation in order to isolate NRBCs for fetal diagnostics.

Simulation results from COMSOL implementation revealed that seven out of ten RBCs successfully traveled to the intended lateral channels while three out of ten traveled through the center channel. All ten WBCs ended up in the center channel as intended. The three RBCs were collected in the middle channel due to their starting position. At the center of the channel before the fork, the magnetophoretic force was very weak and close to zero because magnets from both sides of the channel apply a force on those cells. In order to improve the efficiency of the magnetophoretic separator, the geometry of the channel was changed. An initial bifurcation was implemented that caused unilateral application of the magnetophoretic force before the main channel re-converged. By doing so, the initial force balance was broken and separation efficiency was improved from 70% to 90%.

Additionally, in order to improve device throughput the inlet velocity was subject to optimization. Using an objective function penalizing loss of RBCs and WBC contamination, an optimum inlet velocity of  $0.875 \text{ mm} \cdot \text{s}^{-1}$  was determined. These actions constituted steps in solving the speed and accuracy constraints that have prevented successful commercialization of such a device. In doing so, model validation provided the basis for future manufacturing and testing and satisfied our motivation in developing safer fetal diagnostics.

## 2 Introduction

Prenatal screening and diagnostics are an essential tool in providing fetal medical information to parents and healthcare staff. Such tests have numerous applications, not limited to sex determination, birth defect detection, and the identification of genetic disorders [2]. A number of diagnostic techniques have been developed that fall into two main categories – invasive and non-invasive. Invasive methods involve the insertion of probes into the uterus and the sampling of fetal tissue. Examples include amniocentesis, the extraction of amniotic fluid, and chorionic villi sampling, the extraction of placental tissue. Because invasive techniques result in fetal DNA, they have robust diagnostic potential; however, they necessitate the risk of fetal trauma, infection, and miscarriage [2]. Non-invasive techniques, such as ultrasonography, carry little risk to the fetus but are generally unable to provide definitive diagnoses. For this reason, they are often used only as screening methods and followed by an invasive test to confirm any initial diagnoses.

In light of this, recent research has explored the detection and isolation of fetal cells known to be present in maternal circulation. Successful isolation of such cells may allow the extraction of fetal DNA through non-invasive means, providing greater diagnosing clout without the adjoining risk of conventional procedures. To emphasize this risk, procedures such as trans-cervical chorionic villus sampling carry a 9.4% risk of spontaneous miscarriage [3]. Therefore, a non-invasive means of harvesting fetal DNA strongly fulfills a medical need for safer fetal diagnostics.

We seek to obtain a model that samples fetal cells from maternal circulation by taking advantage of differing material properties. While most cells are diamagnetic (repelled by magnetic fields), deoxygenated adult and fetal red blood cells (RBCs) are paramagnetic (attracted by magnetic fields) when immersed in blood plasma. This is due to gains in magnetic susceptibility native to hemoglobin reduction [1]. Therefore the difference in magnetic properties of RBCs from other cells provides a discrimination criterion for a magnetophoretic separation process. Because fetal RBCs are nucleated while maternal RBCs are not, separation of RBCs from other blood constituents provides an appropriate genetic sample for analysis [4].

The first phase of a lab-on-chip device has been developed that makes use of this concept, though the lack of a rapid and inexpensive solution with great accuracy and efficiency has prevented implementation. By applying a high magnetic field gradient and inducing magnetic forces, RBCs may be isolated from blood in a specially designed microfluidic channel. A model simulation was run using COMSOL Multiphysics. This simulation incorporated magnetics, fluid dynamics, and particle tracing in order to fulfill our objective of optimizing device throughput/yield. As the primary genetic contaminant found in blood, white blood cells (WBCs) acted as the representative constituent we attempted to separate from the desired RBC sample.

### 3 Design Objectives

The proposed structure consisted of a microfluidic channel with soft magnetic elements electrodeposited along its length. Surrounded by permanent magnets providing a proper bias field, the soft magnetic elements locally amplify the magnetic field within the channel to provide a filtering magnetic field gradient. The channel consists of one inlet and three outlets—two lateral ones for the RBCs and one central one for WBCs and other extraneous waste particles. Given this qualitative description of the device our design objectives were to:

- Determine the optimum inlet flow velocity while maintaining separation efficiency.
- Determine the bias field strength appropriate for separation.
- Determine the soft magnetic element size and spacing required to produce a proper magnetic field gradient.
- Determine whether novel geometries can improve throughput while maintaining accuracy.

### 4 Schematic

The microfluidic device consists of a main input channel branching into three equal sized channels near the end of the device. Figure 1, containing a side view and top view of the channel, shows the dimensions of this end region where the trifurcation takes place. In the top view, the input flow would enter from the left, while the output and waste flows exit to the right. The channel has a rectangular cross section that is constant along its length. The magnetic field is constructed with two neodymium magnetics located near the channel. Ni-Fe (Permalloy) magnetic elements line the exterior of the channel walls.

#### 4.1 Device

Approximate dimensions of this end region are given in millimeters. The trifurcation angles are given in degrees. All of these dimensions will be adjusted in optimizing the channel throughput; therefore, this diagram is only for reference to approximate geometries. In addition, the permanent magnets were located closer to the channel for clarity, and the actual channel length before trifurcation was on the order of 10 mm. The geometries along this length will be patterned until trifurcation, as shown in Figure 1.

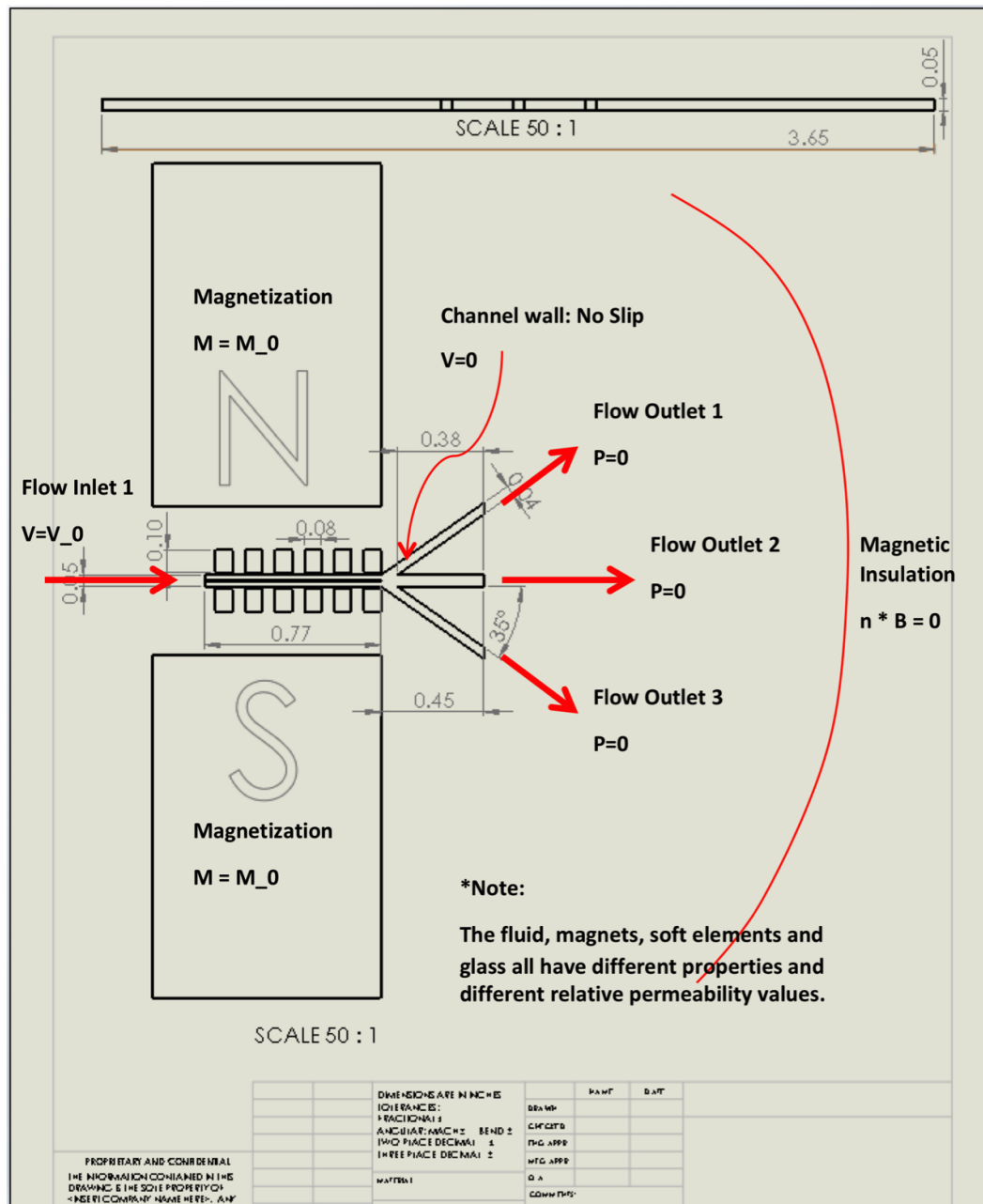


Figure 1: Schematic of the generalized device to be optimized. Note that the boundary conditions and dimensions are labeled accordingly on the figure. The blood to be sampled enters from flow inlet 1. The RBCs will exit from flow outlets 1 and 3, while WBCs and other molecules will exit from flow outlet 2. The magnets and soft elements above and below the channel provide the magnetic field gradient for separation.

## 4.2 Mesh

Using the partial design schematic, a converged mesh was obtained for the complete device. This was accomplished by evaluating the surface integral of the product of magnetic field density and the gradient of the magnetic density over the channel:

$$I = \iint_{\omega} \frac{\partial H^2}{\partial y} dA \quad (1)$$

This parameter was chosen because it is the relevant quantity in computing the magnetic force applied to the particles. Two mesh domains were of interest in the convergence analysis, the structured quadrilateral elements composing the channel domain and the unstructured triangular elements composing the remaining device. Structured elements were implemented within the channel for finer control for adjustments to channel geometry. By plotting the convergence parameter as a function of the number of elements composing the mesh domains, the converged mesh size was determined.

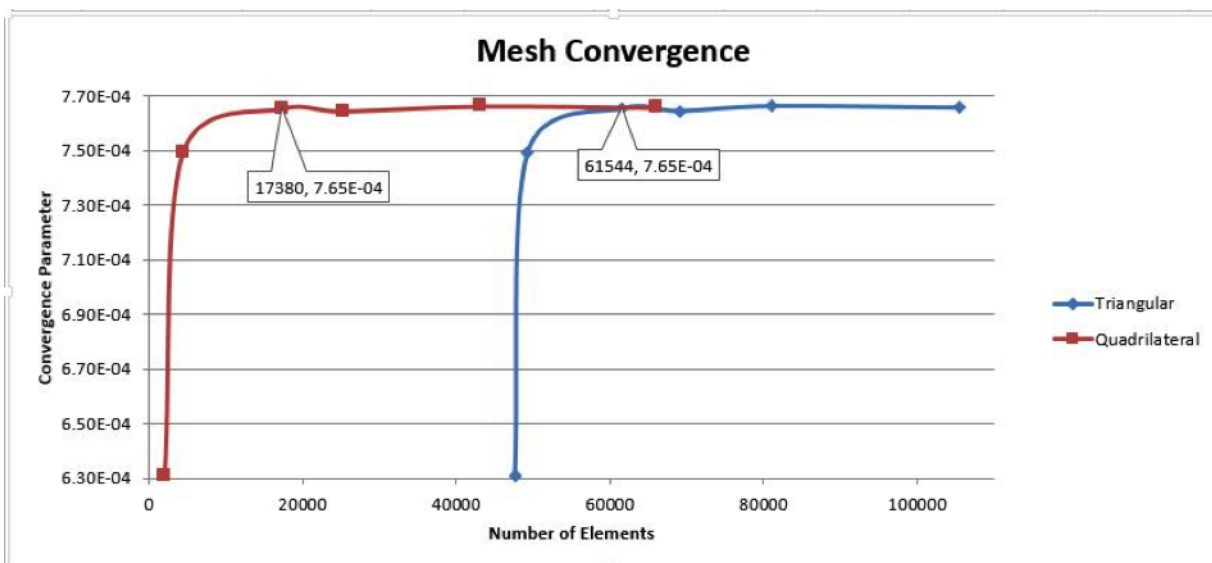


Figure 2: Mesh convergence analysis. Quadrilateral elements make up the channel domain and the triangular elements compose the rest of the device. The plot of the convergence parameter vs. the number of elements displays that the mesh converges at 17,380 quadrilateral elements and 61,544 triangular elements.

An overview of the mesh domains was provided in figures 3 and 4.

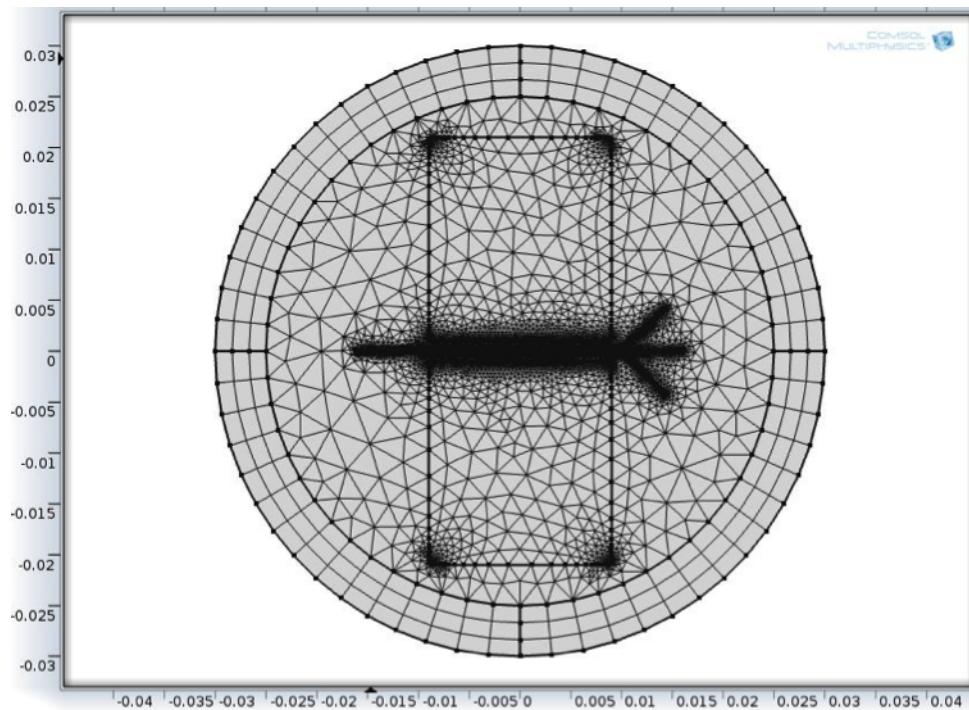


Figure 3: The overall geometry of the magnets, soft elements, and the channel with its fully refined mesh domain. The dark areas constitute significantly refined elements which was necessary in areas of high magnetic field gradient.

Mesh refinement was performed at the corners and channel side faces of the permanent magnets and soft elements because they were the most significant originators of the magnetic field gradient. Additional refinement occurred within the channel. The disparate difference in element size throughout the device obscures the smaller components of the system. Successively magnified views shown in Figure 4 reveal the finer mesh structure.

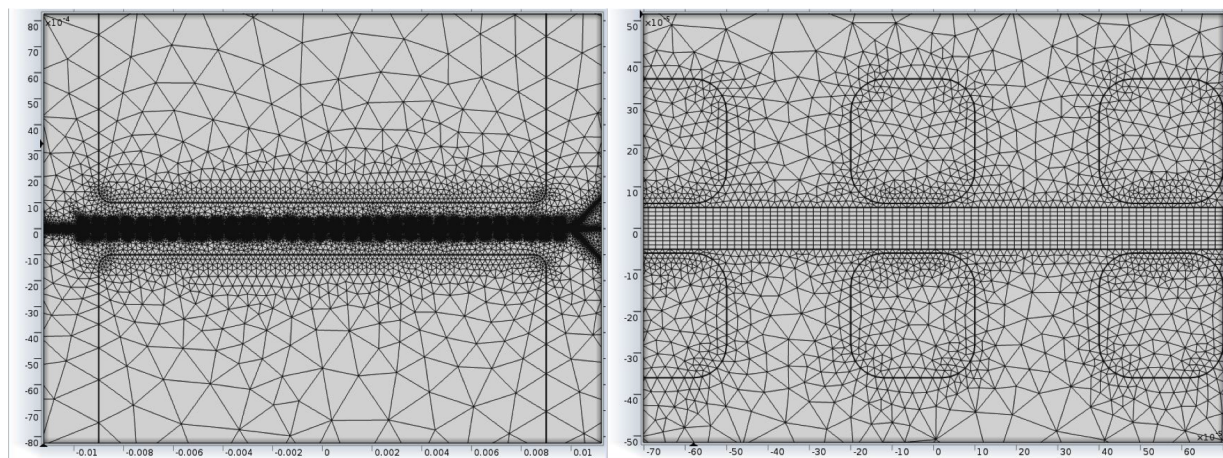


Figure 4: A magnified mesh view. The left displays a magnified view of the the converged mesh. The right displays a further magnified view, presenting the channel and soft element mesh structure.

## 5 Theory

Two physics influence the motion of the cellular blood constituents—magnetostatics and fluid dynamics. The soft magnetic elements electrodeposited along the length of the channel locally amplify the permanent bias magnetic field sourced from the permanent magnets, creating a spatially varying static field pattern. The magnets were positioned such that the field direction was transverse to the channel length, providing a force on the cells perpendicular to the flow. Cellular motion along the channel was governed by drag due to fluid flow. The combination of both governed overall cellular motion, and thus the separation process.

### 5.1 Magnetostatics

#### 5.1.1 Governing Equations

In a magnetostatic situation absent of free electric currents, the differential form of Ampere's reduces to:

$$\nabla \times \vec{H} = 0 \quad (2)$$

The  $\vec{H}$  and  $\vec{B}$  fields are related by the constitutive relation,

$$\vec{B} = \mu_o \vec{H} \quad (3)$$

However, in strongly magnetic materials, the magnetization must be explicitly included using the relation,

$$\vec{B} = \mu_o \vec{H} + \vec{M} \quad (4)$$

The finite element calculation uses a modified form of the magnetostatic equations above in order to calculate magnetic potential. The value of  $\vec{B}$  can be found from the magnetic vector potential. Since the divergence of the magnetic flux density is always zero,

$$\vec{B} = \nabla \times \vec{A} \quad (5)$$

#### 5.1.2 Boundary Conditions

In this study, the magnetic field is symmetric with respect to the xy-plane and antisymmetric with respect to the xz-plane. Thus on the xy-plane, the boundary condition is of magnetic insulation:

$$\hat{n} \cdot \vec{B} = 0 \quad (6)$$

On the xz-plane and at a reference point leftmost from the device, the boundary condition is of zero magnetic scalar potential:

$$\vec{A} = \vec{0} \quad (7)$$

## 5.2 Fluid Dynamics

### 5.2.1 Governing Equations

The incompressible Navier-Stokes equations govern the blood flow through the device:

$$\rho_f \left[ \frac{\partial \vec{u}}{\partial t} + \vec{u} \cdot \nabla \vec{u} \right] - \mu \nabla^2 \vec{u} = -\nabla p \quad (8)$$

A gravitational body force was ignored due to the comparable densities of blood plasma and cells.

### 5.2.2 Boundary Conditions

At the inlet, blood enters at a constant velocity:

$$\vec{u} = u_{in} \hat{i} \quad (9)$$

Because the outlets are exposed to the atmospheric pressure,

$$p_{out} = 0 \quad (10)$$

The walls of the channel have a no slip boundary condition.

## 5.3 Motion

### 5.3.1 Governing Equations

The governing equation for induced cellular motion was Newton's Law:

$$\vec{F} = (\vec{F}_M + \vec{F}_D) = m\vec{a} = m \frac{d}{dt}(\vec{v}_c) \quad (11)$$

Given a region characterized by a magnetic field, the magnetic force on a magnetized body can be expressed by

$$\vec{F}_M = \mu_f(\chi_c - \chi_f)V_c \nabla \vec{H}^2 \quad (12)$$

Assuming RBCs and WBCs may be approximated as spheres, the drag force was predicted by Stokes Law:

$$\vec{F}_D = \frac{18\mu_f}{\rho_c d_c^2} m_c (\vec{u} - \vec{v}_c) \quad (13)$$

## 6 Results

### 6.1 Original Design

Reconstructing the prototype proposed by Schiavone et al, a working model of a separator device was developed. Uncoupled fluid flow and magnetostatic simulations followed and were then coupled to a particle tracking representing the motion of blood cells within the device. Subsequently, input parameters were optimized for throughput and efficiency to improve the initial device and suggest an improved design.

#### 6.1.1 Fluid Simulation

Figure 5 displays the fluid velocity profile in the region of the trifurcation fork. From the velocity contours it was evident that the velocity sharply decreased after passing the trifurcation point, mainly due to the sudden increase in cross-sectional area. As expected, the flow velocity was zero at the walls due to the no-slip boundary condition present there.

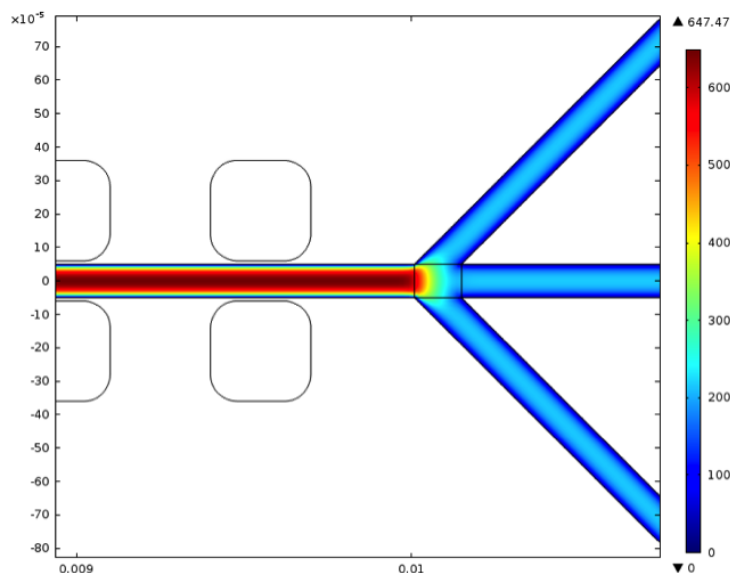


Figure 5: Fluid velocity contour near the bifurcation fork. Significant velocity decrease occurred at outlets due to increased cross-sectional area. Units are in  $\mu\text{m/s}$ .

Fluid pressure was plotted along the center channel in figure 6. Pressure decreases steadily until the trifurcation point was reached, after which the pressure gradient along the channel decreases. This was also due to the increase in cross-sectional area.

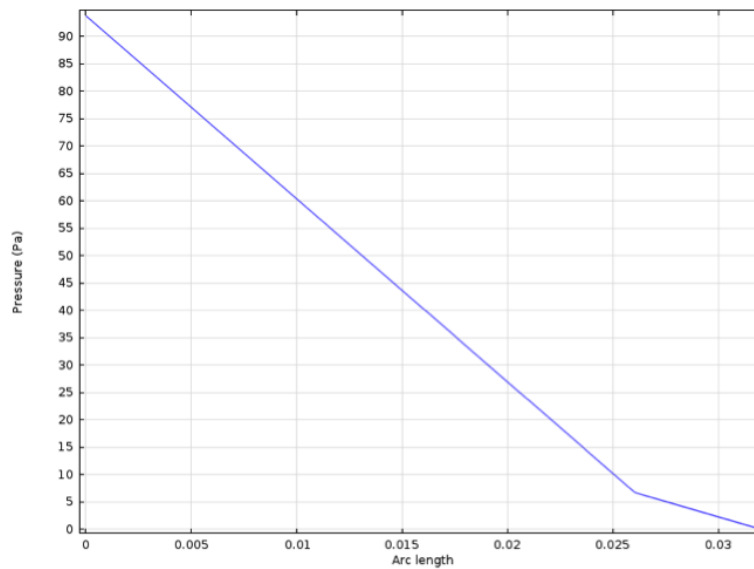


Figure 6: Fluid pressure along center channel. Steady decrease in pressure occurs until the trifurcation fork, at which point the pressure gradient decreases.

### 6.1.2 Magnetic Field Simulation

As demonstrated in figure 7, magnetic flux density is strongly enhanced by the presence of the soft metal deposits. As a result of the periodic deposition of the soft elements, the magnetic flux density in the channel also varies periodically.

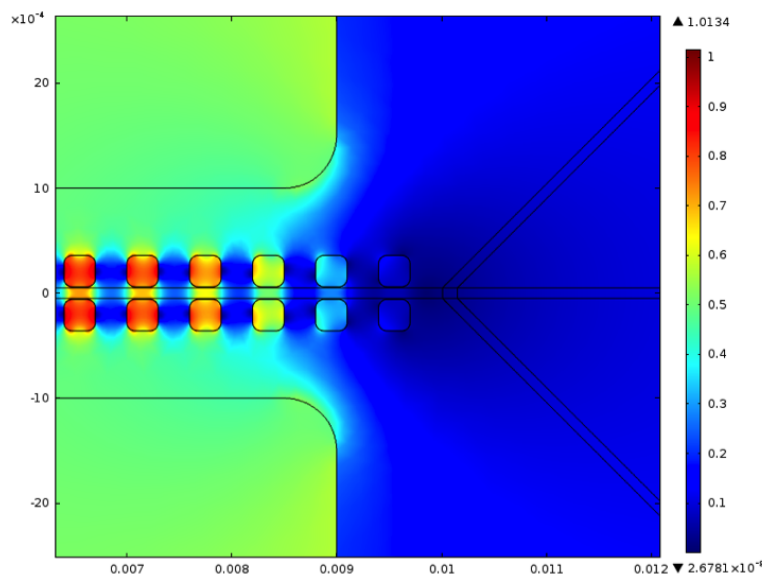


Figure 7: Contour plot of magnetic flux density magnitude,  $|\vec{B}|$ . Note the periodicity along the channel due to the local amplification by the soft elements.

Figure 8 explicitly shows how the magnetic flux gradient applies a magnetophoretic force to the blood cells. Because the applied force is proportional to the gradient squared, a stronger gradient magnitude (positive, red; negative, blue) results in a stronger magnetophoretic force. This plot also reveals that the edge of the soft element is the source of the strongest magnetic flux gradient and that away from the soft elements the gradient is zero.

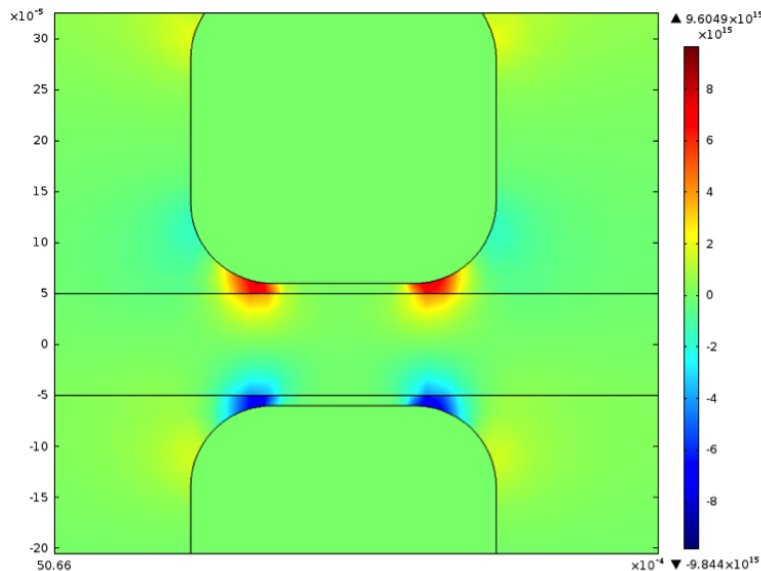


Figure 8: Contour plot of the y-component of magnetic flux density gradient. Note the increase magnitude near the soft element corners and the symmetry about the center line.

### 6.1.3 Particle Tracing

Particle tracking was conducted with an equidistant drop of ten particles, each of which was performed independent of the other. From the particle tracks in figure 9, the path deflections confirmed that application of a magnetic flux gradient forced RBCs across streamlines to the channel walls while converging the WBCs to the center of the channel. The force applied was greatest in proximity the the channel walls as expected from the gradient indicated in figure 8. Force magnitude was zero at the center of the channel, providing the conditions necessary to maintain center position of the WBCs.

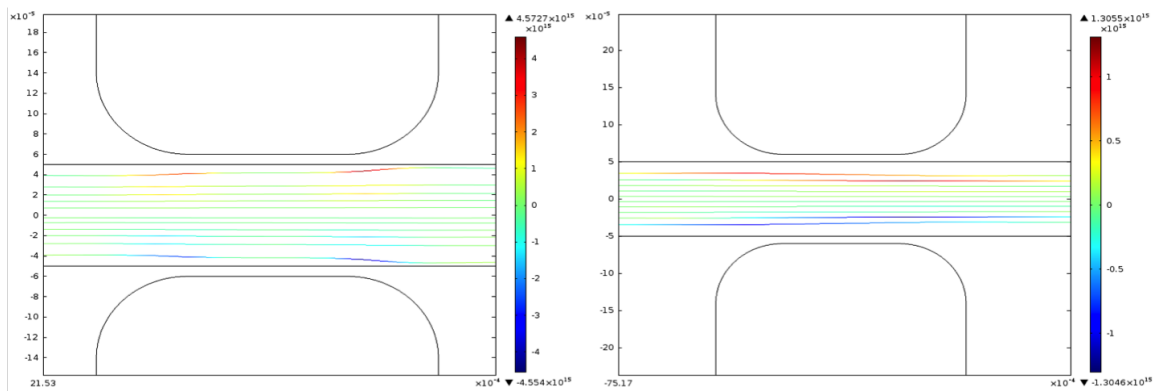


Figure 9: Particle tracks of red blood cells (left plot) and white blood cells (right plot) near the region between two soft metal elements. The coloring shows the magnetophoretic force applied to the particles.

From observation of particle tracks exiting the device, figure 10 shows that most of the RBCs (seven out of ten) exited the side channels, while a portion of them (three out of ten) exited via the center waste channel. Furthermore, all of the WBCs were successfully funnelled into the center channel. It is important to note that in the RBC case, it may seem that less cells exited the device than were released. This was due to the no slip wall conditions implemented in the model, which effectively halted progress of some cells in close proximity to the channel walls. Particles that have stopped short of the outlet due to this condition are expected to exit via the side channels regardless. They are deemed separated because they will subsequently roll along the wall until the end of the main channel, at which time drag forces will push them out the proper outlet along the streamlines [4]. Additional support for this proposition may be found in section 8.1.

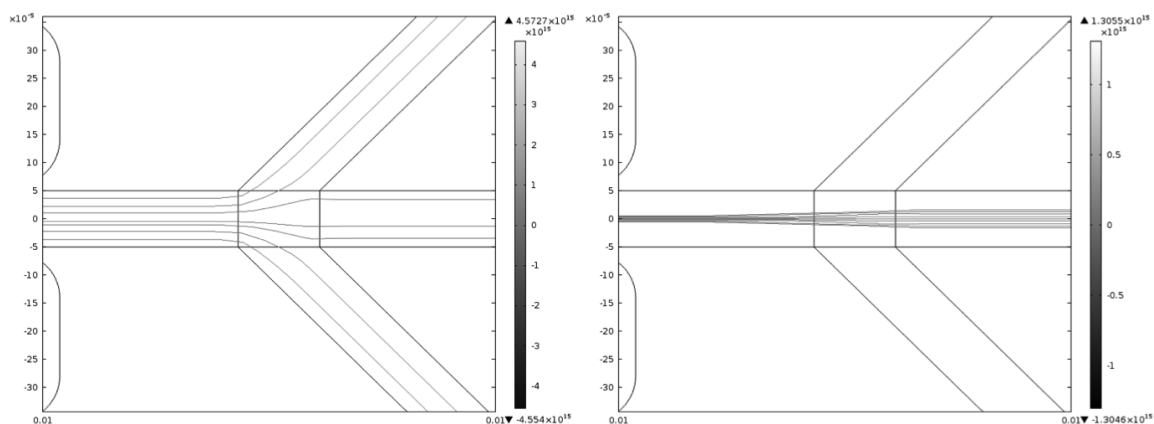


Figure 10: Particle tracks of red blood cells (left plot) and white blood cells (right plot) near trifurcation. Note that there is a total injection of ten particles, hence in the left plot all the other particles slowed by contact with the channel wall are assumed to exit the side channels.

## 6.2 Flow Rate Optimization For Efficient Throughput

Without changing the original design, we can test for different inlet velocities. A faster throughput would save more time, which is desirable, but could result in a greater loss in RBCs and WBCs. With a larger throughput velocity, the blood cells might not have enough time to appropriately respond to the magnetophoretic forces, resulting in a poorer separation. Likewise, WBCs on the channel peripheral might remain there by the time the outlets are reached when a greater velocity is applied. An objective function is defined and utilized to find the optimal flow velocity.

### 6.2.1 Objective Function

The objective function is based upon three variables,  $u_{in}$ ,  $L_w$ , and  $L_r$ . In the simulation trials, the flow inlet velocity is the independent variable and the red blood cell and white blood cell loss are dependent variables. A bonus is given for a larger flow velocity, while a penalty is given for loss of blood cells. Due to the later separation processes, a loss of red blood cells is not very serious, while a mix of white blood cells into the separated red blood cells is highly undesirable. Hence in the objective function, a higher penalty is given for white blood cells. The objective function is given below:

$$\begin{aligned}\Phi(u_{in}, L_w, L_r) &= K_{fv} * u_{in} + K_{wbc} * L_w + K_{rbc} * L_r & (14) \\ K_{fv} &= 1 [s \cdot mm^{-1}] \\ K_{wbc} &= -5 \\ K_{rbc} &= -1\end{aligned}$$

In equation 14,  $K_{fv}$  is a boost factor for flow velocity,  $K_{wbc}$  and  $K_{rbc}$  are the penalty factors for loss of WBCs and RBCs respectively,  $u_{in}$  is the inlet velocity, and  $L_w$  and  $L_r$  are the loss rate of WBCs and RBCs respectively. Weights were chosen to reflect that loss of some RBCs was acceptable, but contamination by WBCs was not.

### 6.2.2 Results from Objective Function Evaluation

Simulations were performed with a range of inlet velocity values, ranging from  $0.5 \text{ [mm} \cdot \text{s}^{-1}]$  to  $1.5 \text{ [mm} \cdot \text{s}^{-1}]$ . 50 RBCs or WBCs were released for each simulation. By maximizing  $\Phi$ , the optimum inlet velocity may be obtained.

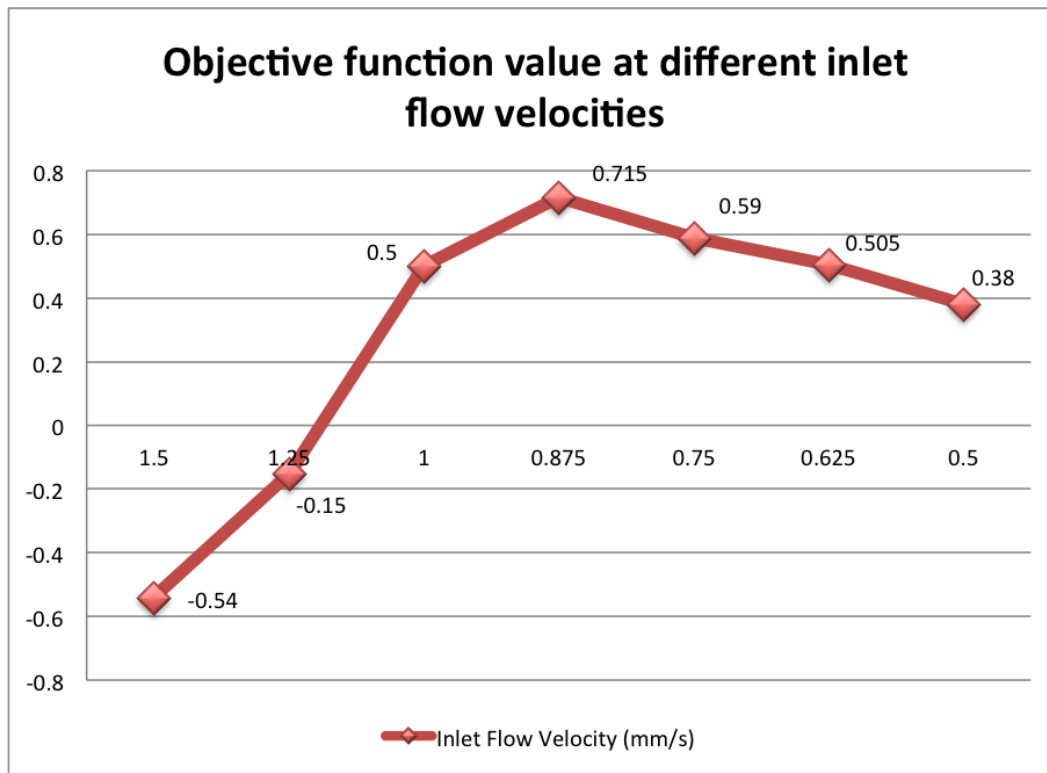


Figure 11: Plot of objective function at different flow velocities. Maximizing the objective function yields an optimum throughput of  $0.875 \text{ [mm} \cdot \text{s}^{-1}]$ .

Based on the analysis of the objective function values, optimal throughput was achieved at an inlet flow velocity of  $0.875 \text{ [mm} \cdot \text{s}^{-1}]$ , where the objective function value  $\Phi$  has a peak value of 0.715.

### 6.3 New Design with New Flow Channel Geometry

Rather than changing design parameters from the original design, a flow channel with significantly different geometry has been simulated. As a result of the force balance from both sides of the channel, it is not possible to separate the red blood cells right at the center line using magnetophoretic forces. In lieu of this analysis, a new design with bifurcating and then reuniting flow channel was proposed.

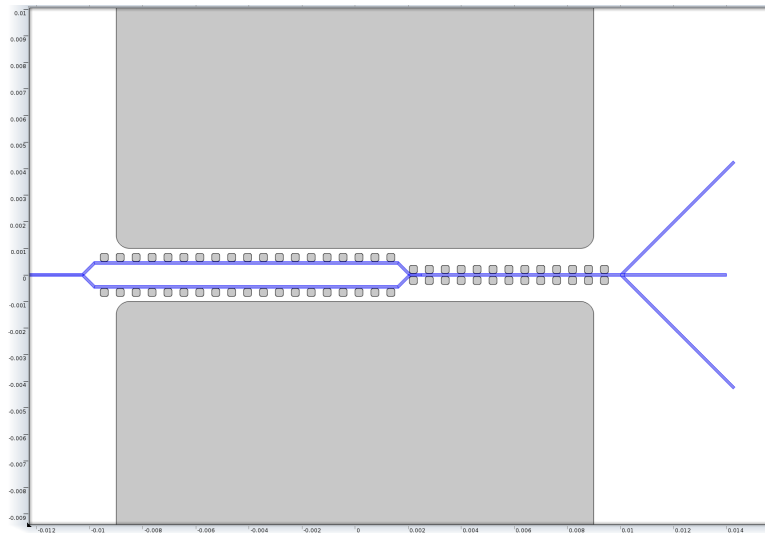


Figure 12: Geometry of new design. Flow channels take a different geometry from the original design. Initially the flow channels bifurcate and then converge in order to apply unilateral force.

Within the parallel channels of the new design, the cells are affected by a unilateral side force due to the unilateral placement of soft elements. Hence, any RBCs originally in the center channel are forced to the bottom of the channel, causing migration to the main channel wall after the bifurcation reunites. After the channels converge, RBCs will stay away from the center line due to the greater force magnitude in proximity to the channel walls, therefore promoting a better separation for RBCs.

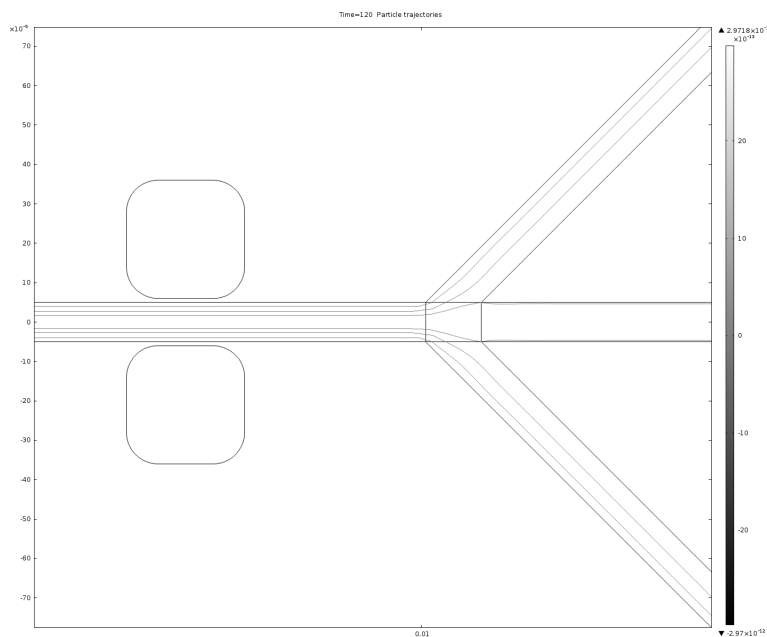


Figure 13: Red blood cell separation results for the new design. With an initial injection of twenty RBCs, only two are lost to the center channel. A success rate of 90% can be achieved.

Simulation results based on this new design are shown in figure 13. Of the initial injection of twenty RBCs, only two are lost to the center outlet. This proves a success rate of 90% separation for RBCs, compared to a 70% separation success rate for the original design with the same inlet flow velocity. A more careful observation of the two RBCs shows that they nearly made it to the side channels. Hence in regard to RBC separation, the new design functions much better than the original design. Geometry changes, such as channel lengthening, should lead to complete separation.

## 7 Sensitivity Analysis

### 7.1 Parameters to Adjust

With this device, input parameters have significant variability. Most importantly, the blood samples obtained might have varying dynamic viscosity and density. In addition, magnetic field strength of the neodymium permanent magnets may vary across manufactured devices. Finally, the soft element deposition process could result in inconsistently sized soft elements. Therefore, it will be useful to analyze the effect of variation in blood composition, magnetic field strength, and soft element width on the efficacy of our magnetophoretic separator. For each of these tests, we will use a magnetophoretic separator with input flow rate of  $.875 [mm \cdot s^{-1}]$ , our optimized flow rate.

### 7.2 Sensitivity to Input Parameters

#### 7.2.1 Blood Viscosity

Blood dynamic viscosity values are in the range of  $3 - 4 [mPa \cdot s^{-1}]$  [5]. A simple analysis on the effect of blood viscosity on separation efficacy was performed using the boundary values of this range. For normal simulation, a blood viscosity of  $3.5 [mPa \cdot s^{-1}]$  was used. At both  $3 [mPa \cdot s^{-1}]$  and  $4 [mPa \cdot s^{-1}]$ , an identical number of RBCs exited the proper outlet channels and all WBCs exited through the center waste channel. Therefore, viscosity variation within normal biological limits had no observable effect on the separation efficiency of this device.

#### 7.2.2 Blood Density

At both 90% blood density and 110% blood density, no changes in separation efficiency were observed.

#### 7.2.3 Magnetic Field Strength

The magnetization of the permanent neodymium magnet used in our model was  $M_o = 6 * 10^5 A \cdot m^{-1}$ . In order to determine the effect of variation in magnet quality, we compared field strengths of  $6 * 10^5 \pm 10\%$ . At 90% magnetization, more RBCs were lost to the waste channel and more WBCs to the side channels. This was likely due to a decreased magnetic gradient across the channel,

resulting in a lower separation force. At 110% magnetization, we saw no changes in separation efficiency.

### 7.2.4 Soft Element Width

The width of the soft elements used in our model was  $300 \mu m$ . In order to determine the effect of variation in soft element deposition, we looked at widths of  $300 \mu m \pm 10\%$ . At 90% width (or around 81% total area), we saw no changes to separation efficiency. At 110% width (or around 121% total area), we lost a couple more RBCs to the center waste channel.

## 7.3 Sensitivity Summary

As summarized in table 1, minor changes in blood viscosity and density have no observable effect on the separation efficiency of our device (evaluated using our objective function). However, when using a low magnetization, a significant penalty in the objective function was observed. This was caused primarily by the presence of white blood cells in the side channels. Small variations in soft element deposition also affected evaluation of the objective function, but not as significantly as magnetization of the permanent magnets. Therefore, it is crucial to maintain the appropriate magnetization when designing a magnetophoretic separator. With the proposed geometry, we would recommend not using a neodymium magnet with magnetization properties below the  $6 * 10^5 A/m$  threshold.

Parameter	Range	Objective Function Range
Blood Viscosity	$3 - 4 mPa/s$	.715-.715
Blood Density	$900 - 1000 kg/m^2$	.715-.715
Magnetization	$5.4 - 6.6 \times 10^5 A/m$	.075-.715
Soft Element Width	$270 - 330 \times 10^{-6} m$	.675-.715

Table 1: Sensitivity analysis summary. For each parameter, simulations were run at the boundaries of the parameter range. Objective functions at those values were calculated and are presented here as a range.

## 8 Accuracy Check

To ensure our model was correctly implemented with respect to the specifications and assumptions required and accurately represented a real physical system, verification and validation procedures were conducted. Structural assumptions concerning the fluid flow character and particle tracing were substantiated by analysis of dimensionless numbers corresponding to the behavior of the fluid and the particles. Comparison with previous work was used to validate the numerical model as an efficacious approximation of reality.

## 8.1 Verification

The utility of the devices ability to separate blood cells relied on Stokes flow, a type of fluid flow where advective inertial forces are small compared to viscous forces. That is,  $Re \ll 1 (\leq 0.1)$ . The presence of any turbulence would render the the whole concept moot.

Using characteristic values for the parameters involved in the study,

$$Re \approx \frac{\rho_f u L}{\mu_f} = \frac{(1000 \text{ kg} \cdot \text{m}^{-3})(0.5 * 10^{-3} \text{ m} \cdot \text{s}^{-1})(50 * 10^{-6} \text{ m})}{(3.5 * 10^{-2} \text{ Pa} \cdot \text{s})} \rightarrow Re \approx 0.0007$$

The flow type was shown to be well within the range of Stokes Flow. Because the Reynolds number calculated was magnitudes below the required condition, Stokes flow should be maintained in all possible parameter sweeps conducted in the sensitivity analysis. However, even with Stokes flow the particles may not perfectly advect down the fluid streamlines. Sufficient particle inertia may cause a particle to continue along its initial trajectory at directional changes in the streamlines, such as the diverging outlets.

The behaviour of the cells suspended in the blood may be characterized by Stokes number ( $Stk$ ), the ratio of the characteristic time of a particle to the characteristic time of the flow:

$$Stk = \frac{t_o u_f}{L} \text{ where } t_o = \frac{\rho_c d_c^2}{18\mu_f} \text{ in the case of Stokes flow.}$$

This is equivalent to determining the balance between the advective and inertial response of the particles, therefore the Stokes number may be used as a measure of flow tracer fidelity, i.e., how closely particles follow fluid streamlines [6]. Smaller Stokes numbers correspond with better tracking accuracy.

For  $Stk \gg 1$ , particles detach from a flow at places in which the flow decelerates abruptly, such as the channel outlets. For  $Stk \ll 1$ , particles follow fluid streamlines closely and for  $Stk \ll 0.1$ , tracing accuracy errors are below 1% [7]. Thus, failure to achieve  $Stk \ll 1$  would invalidate the model. Using the applied parameters:

$$Stk = \frac{u \rho_c d_c^2}{18\mu_f L} = 0.006$$

Thus, complete tracing fidelity may be safely assumed. RBCs contacting the channel walls will track out the outlets, following the appropriate streamlines. One oversight was the inverse effect of the particles on the velocity field of the fluid flow due to the comparable size of the channel width in comparison to cell diameter ( $\approx 10 : 1$ ). Such considerations were beyond the scope of this paper but were safely assumed in previous work [4].

## 8.2 Validation

Comparisons between results from this study and published results (Shiavone et.al.) have been made to validate the model. Comparisons are made for magnetic flux density along channel length, magnetophoretic force (y-component) along channel length as well as magnetophoretic force (y-component) along channel width.

As demonstrated by data overlap in figure 14, agreement in amplitude and periodicity was observed between our model and the literature for magnetic flux density along the main channel length.

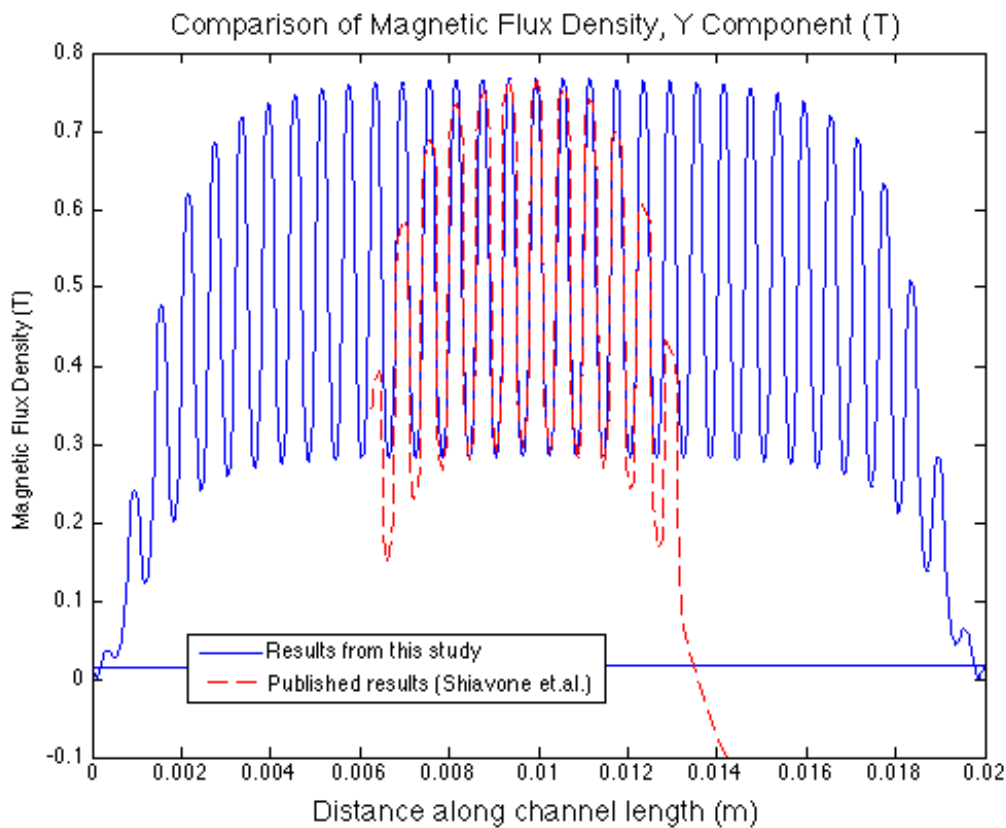


Figure 14: The y-component of the magnetic flux density,  $B_y$ , along the channel length. This field is the superimposition of the bias field from the magnets and the local amplifications due to magnetization of the soft elements. Comparison with Schiavone et al model demonstrates agreement in amplitude and periodicity, though our model occurs over a greater length.

Strong agreement in force magnitude along the main channel length was observed as well, as illustrated in figure 15.

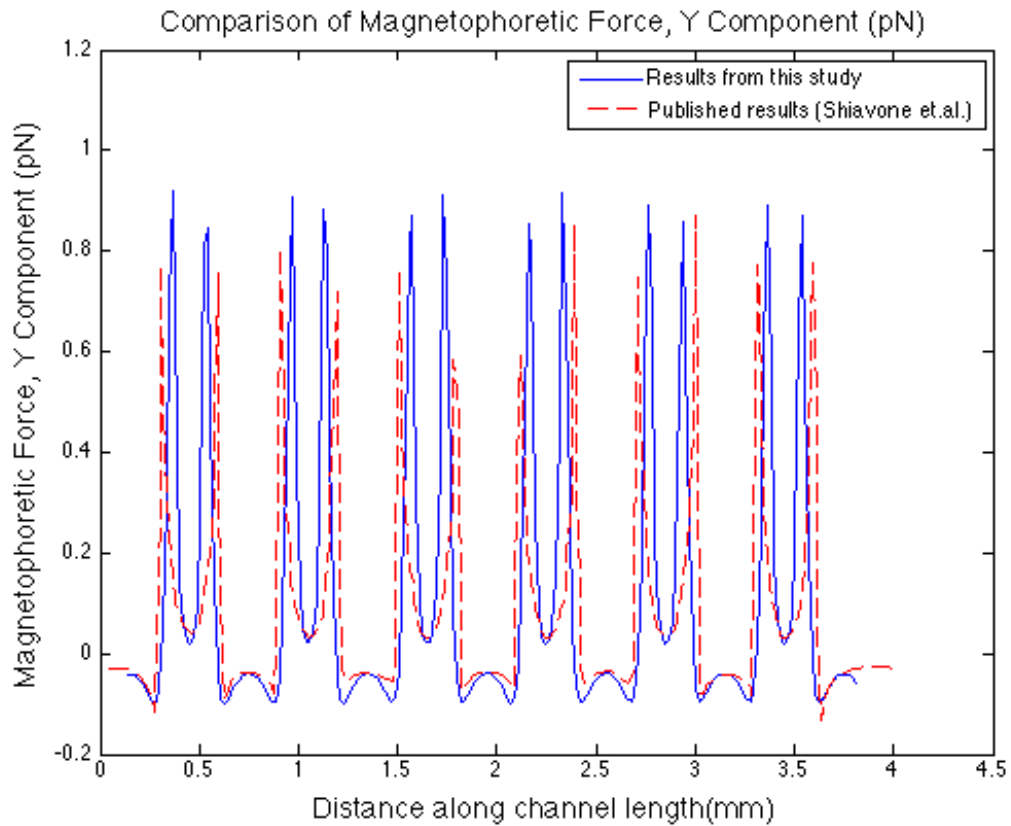


Figure 15: The transverse component of the magnetic force,  $F_{m,y}$ , along the channel length. Overlap with data from Schiavone et al model confirms that the net force was sufficient to force RBCs towards the channel wall as expected.

As supported in figure 16, agreement in force magnitude across the channel width solidifies congruence of our model with that found in the literature.

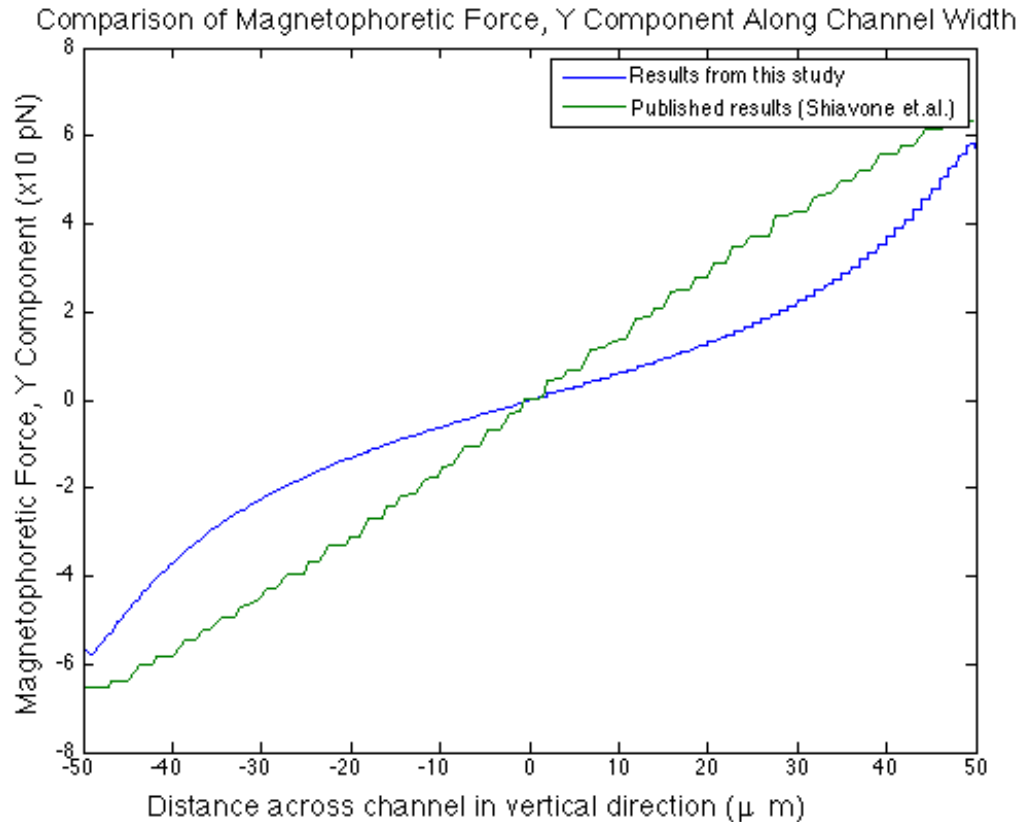


Figure 16: The transverse component of the magnetic force,  $F_{m,y}$ , across the channel for a position corresponding to the center of a soft element. Force magnitude is greatest at the channel walls and zero at the center. Our model has a less linear change in magnitude, but is validated by having an identical amplitude and behaviour as the Schiavone et al model. The sign of force switches crossing the centerline of the channel, underpinning an unstable equilibrium point which allows for separation.

## 9 Conclusion

A successful model of a fetal cell magnetophoretic separator was implemented in COMSOL. The model demonstrates the feasibility of a non-invasive lab-on-chip device for fetal diagnostics. Concepts from previous works were expanded on and optimized for throughput, improving the need for speed and efficiency. Along with an improved design, the validated model paves the way for future manufacturing and testing. Results of will constitute another step in the development of improved pregnancy healthcare.

## 9.1 Future Work

There is much future work needed in order to develop an ideal working device. Optimal geometric dimensions are still in question. Future work may entail determining the optimum channel width, determining the effect outlet angles have on successful separation, and determining the minimum separation length required that guarantees complete separation. Additionally, the model relied on two assumptions that may not be valid. The drag force equation (defined for spheres) was applied to non-spherical RBCs with an equivalent radius. The presence of cells was also assumed not to influence local flow conditions or field strength. A more accurate model would incorporate a more suitable drag force and couple the cells motion to that of the fluid dynamics and magnetostatics.

## 10 Contributions

### Zachary Flood

- Executive Summary and Introduction
- Mesh Convergence
- Theory
- Verification
- Appendices, Conclusion and Future Work
- Latex implementation, document formatting/editing, figure captioning

### Naveen Jasty

- Sensitivity Analysis
- Designing and performing the simulation for the original model
- Schematic
- Figures

### Chiyu Jiang

- Performing parts of the simulation for the original model.
- Designing and performing simulations on the new model.
- Evaluation of objective function.
- Validation of the result by performing comparisons with publish studies.

### Jino Park

- Composing and updating the Executive Summary and Introduction.
- Completing the captions for the figures.
- Finding and citing references.
- Preparing presentation slides.

## 11 Appendices

### 11.1 Input Parameters

Parameter	Description	Value
$\mu_o$	Permeability of Free Space	$4\pi * 10^7 N \cdot A^{-2}$
$\rho_c$	Cell density	$1125 kg \cdot m^{-3}$
$\rho_f$	Fluid Density	$1000 kg \cdot m^{-3}$
$\mu_f$	Fluid Viscosity	$3.5 mPa \cdot s$
$M_o$	Magnetization	$6 * 10^5 A \cdot m^{-1}$
$d_{cr}$	Diameter of RBCs	$6 \mu m$
$d_{cw}$	Diameter of WBCs	$12 \mu m$
$\chi_r$	Magnetic Susceptibility of RBCs	$3.9 * 10^{-6}$
$\chi_w$	Magnetic Susceptibility of WBCs	$9.2 * 10^{-6}$
$\chi_f$	Magnetic Susceptibility of fluid	$7.7 * 10^{-6}$
$L$	Characteristic Length	$50 \mu m$

Table 2: Input Parameters

### 11.2 Variable Definitions

Variable	Units	Definition
$\vec{B}$	T	Magnetic Flux Density
$\vec{A}$	$V \cdot s \cdot m^{-1}$	Magnetic Vector Potential
$\vec{M}$	$A \cdot m^{-1}$	Magnetization
$\vec{H}$	$A \cdot m^{-1}$	Magnetic Field Intensity
$\vec{u}$	$m \cdot s^{-1}$	Blood Velocity
$p$	Pa	Blood Pressure
$I$	$A^2 \cdot m^{-1}$	Convergence Parameter
$\hat{n}$	Dimensionless	Normal Vector
$\vec{v}_c$	$m \cdot s^{-1}$	Cell Velocity
$\vec{V}_c$	$m^3$	Cell Volume
$m_c$	kg	Cell Mass
$t_o$	s	Relaxation Time

Table 3: Variable Definitions

## References

- [1] Lama Sakhnini and Rula Khuzae. “Magnetic behavior of human erythrocytes at different hemoglobin states”. In: *European Biophysics Journal* 30.6 (2001), pp. 467–470.
- [2] Draborg Eva Pedersen Claus D. Hansen Helle P. Lamont Ronald F. Jrgensen Skjth Mette M. and Jan S. “Providing information about prenatal screening for Down syndrome: a systematic review”. In: *Acta Obstetricia et Gynecologica Scandinavica* 94.2 (2015), pp. 125–132.
- [3] Brigham S. Alfirevic Z. Sundberg K. “Amniocentesis and chorionic villus sampling for prenatal diagnosis.” In: *Cochrane Database Syst Rev* 3 (2008).
- [4] *Design and Simulation of a Microscale Magnetophoretic Device for the Separation of Nucleated Fetal Red Blood Cells from Maternal Blood*. COMSOL Conference.
- [5] G. Elert. *Viscosity. The Physics Hypertextbook*.
- [6] Christopher E. Brennen. *Fundamentals of multiphase flow (Reprint. ed.)* Cambridge University Press., 2005.
- [7] Alexander Yarin Cameron Tropea and John Foss. *Springer Handbook of Experimental Fluid Mechanics*. Springer.